1. Award #: DE-FG02-05ER46250
Institution: Cornell University.

2. Dates: Date of report: August 1, 2013.

3. Title: Transport Phenomena and Interfacial Kinetics in Planar Microfluidic Membraneless Fuel Cells

P.I.: Héctor D. Abruña, Chemistry and Chemical Biology, Cornell University
co-P.I.: Abraham D. Stroock, Chemical and Biomolecular Engineering, Cornell University

4. Final Report

Abstract:
Our work is focused on membraneless laminar flow fuel cells, an unconventional fuel cell technology, intended to create a system that not only avoids most typical fuel cell drawbacks, but also achieves the highest power density yet recorded for a non-H_2 fuel cell. We have employed rigorous electrochemistry to characterize the high-energy-density fuel BH_4^-, providing important mechanistic insight for anode catalyst choice and avoiding deleterious side reactions. Numerous fuel cell oxidants, used in place of O_2, are compared in a detailed, uniform manner, and a powerful new oxidant, cerium ammonium nitrate (CAN), is described. The high-voltage BH_4^-/CAN fuel/oxidant combination is employed in a membraneless, room temperature, laminar-flow fuel cell, with herringbone micromixers which provide chaotic-convective flow which, in turn, enhances both the power output and efficiency of the device. We have also been involved in the design of a scaled-up version of the membraneless laminar flow fuel cell intended to provide a 10W output.

5. Research Findings

A.Electroanalytical investigation of borohydride (BH_4^-): Oxidation mechanism, best catalysts, and performance optimization.

Our search for a highly soluble fuel for microfluidic fuel cell applications quickly focused on BH_4^-, most commonly used as its sodium salt, $NaBH_4$. This compound has considerable solubility in aqueous solutions (>14 M), a high electron recovery per molecule ($8e^-$, Reaction 1), a very low potential for oxidation in base (–1.44 V vs. Ag/AgCl), and extremely fast kinetics at room temperature:

Reaction	E°' (V vs. Ag/AgCl, 1M NaOH)
$BH_4^- + 8OH^- \leftrightarrows 8e^- + H_2BO_3^- + 5H_2O$	–1.44

Reaction 1

Thus, it has approximately the same low onset potential for oxidation as H_2, allowing for high voltage systems. However, because of its very high solubility, about 14,000 times that of H_2, it can have a theoretical maximum current density that is multiple orders of

magnitude greater. $NaBH_4$ also has significant specific and volumetric energy density (9.4 kWh/kg, 10 kWh/L for combustion with O_2), exceeding the values for the much more intensively studied fuel methanol (MeOH; 6.1 kWh/kg, 4.8 kWh/L). While MeOH ($6e^-$, -0.4 V vs. Ag/AgCl in base) would appear similar to $NaBH_4$ based on these thermodynamic, theoretical measures, a comparison of activity yields a very different conclusion. Figure 1 shows RDE voltammograms for the room-temperature oxidation of $NaBH_4$ and MeOH at their best known catalysts, Pt and PtRu, respectively. $NaBH_4$ exhibits a current density *200 times greater* than MeOH, producing 10 times the current at 20 times lower concentration. Thus, it is clear that thermodynamics alone cannot predict the activity of a fuel, and that $NaBH_4$ represents a significantly more power-dense fuel than either H_2 or MeOH.

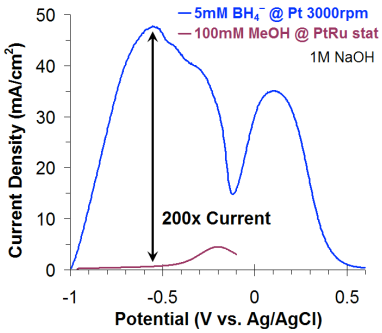

Figure 1: Comparison of 5 mM BH_4^- vs. 100 mM MeOH, both in 1 M NaOH

Though BH_4^- has many attractive features as a fuel, its utilization is hindered by its deleterious hydrolysis reaction, which decomposes the fuel to H_2 and boric acid (Reaction 2).[1,2] Hydrolysis can proceed partially or completely, converting any number of BH_4^-'s eight reducing equivalents to H_2 or partial fractions thereof. Hydrolysis occurs readily in bulk solution, in both acidic and neutral aqueous environments, as well as at the surfaces of various catalysts. Hydrolytic decomposition at electrode surfaces is especially detrimental, as H_2 bubbles block electrodes for further reaction, decreasing the effective surface area of fuel cell catalysts, and disrupt laminar flow across the electrode. Once H_2 is formed, the solubility of the reducing equivalents dramatically decreases, eliminating one of BH_4^-'s principal advantages as a fuel. Thus hydrolysis must be avoided in BH_4^- fuel cell technologies.

BH_4^- Hydrolysis:

$$BH_4^- + H^+ + 2H_2O \rightarrow HBO_2 + 4H_2$$

Reaction 2

Prior to our studies, it was generally accepted in the literature that Au was an ideal catalyst for BH_4^- oxidation, providing all $8e^-$ while precluding hydrolysis.[3,4] In contrast, Pt was reported and believed to hydrolyze BH_4^- extensively, and often provide only 4 to $6e^-$.[5] Moreover, all of the low-potential current at Pt was attributed to H_2 produced from electrolysis, and only the current at high potentials was thought to originate from the direct oxidation of BH_4^-. However, nearly all of these previous

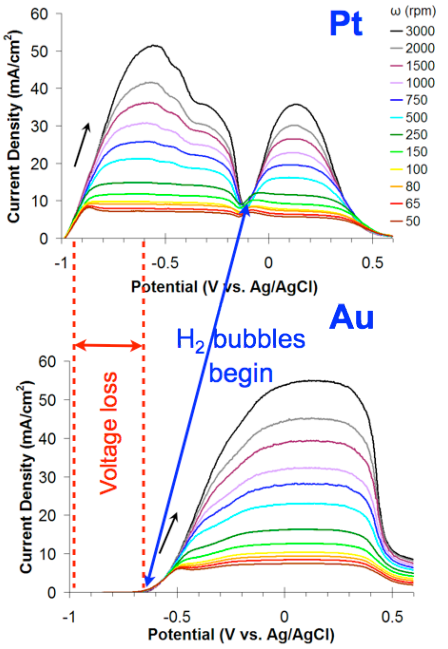

Figure 2: Comparison of BH_4^- oxidation at Pt vs. Au. RDE voltammograms of 5mM $NaBH_4$ in 1M NaOH are shown for each electrode.

studies employed techniques that were not well-suited to establishing mechanistic parameters for fuel oxidation.

To gain an in-depth understanding of the mechanistic details of the oxidation of BH_4^- at Pt and Au electrode catalysts, we employed rotating-disk electrode (RDE) voltammetry, which readily allows distinction between surface-adsorbed and diffusional processes, as well as the determination of kinetic reaction rates and mass transport parameters for a given fuel.[6] Our RDE study represents the first, and we believe the most rigorous, to date, comparison between Pt and Au catalysts for BH_4^-, and provides a fully different (relative to conventional views) perspective on BH_4^-'s oxidation mechanism.[7] Two distinct oxidative reactions were observed at Pt: The first occurred at low potentials (between -1 to -0.1 V vs. Ag/AgCl, Figure 2), and corresponded to a $7e^-$ oxidation of BH_4^-, while the second reaction occurred at higher potentials (-0.1 to +0.3 V), and involved only 5.5 e^-. Contrary to literature reports, Pt's low potential current was directly derived from BH_4^-, rather than H_2, as H_2's solubility is insufficient to produce the high currents involved. That is, our 5 mM fuel gave $7e^-$ in its oxidation, generating a current corresponding to 35 mM e^- equivalents, while H_2, with <1 mM solubility and only 2 e^- available, could produce, at most, a current equivalent to ~2 mM e^- equivalents (assuming comparable diffusion coefficients). Additionally, the current from BH_4^- at low potentials scaled perfectly linearly with $[BH_4^-]$, as the limiting current at 3000 rpm increased from 50 mA/cm^2 to **0.5 A/cm^2**, (specific surface area), when increasing $[BH_4^-]$ from 5 to 50 mM (Figure 3). Such high current densities and quantitative scaling suggest that direct BH_4^- oxidation at low potentials is even more likely, and the sheer current density available makes the low-potential BH_4^- oxidation at Pt a highly attractive fuel oxidation process to harness.

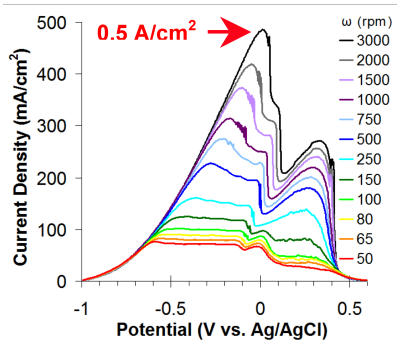

Figure 3: RDE voltammograms for 50 mM $NaBH_4$ in 1M NaOH at Pt, showing current scaling to 0.5 A/cm^2.

Au also exhibited two oxidation processes, with the one at low potentials (-0.6 to -0.3 V) yielding about 4.5 e^-, and the one at higher potentials (-0.2 to +0.4 V) providing the expected 8 e^- (Figure 2). Not only did Pt provide nearly equivalent e^- recovery at lower potentials (which would result in a higher fuel cell voltage) than Au, but the onset potential was about 400 mV more negative. Thus, the use of Pt instead of Au as an electrode will increase the open-circuit voltage of a BH_4^- fuel cell by 400 mV, and its operating voltage (tuned to a potential of maximal e^- recovery; highest power) by 600 mV, while providing close to full recovery of BH_4^-'s $8e^-$.

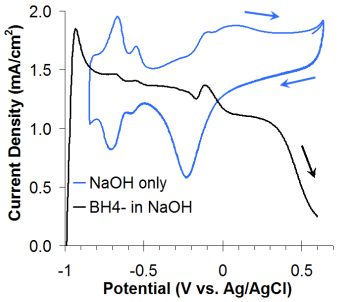

Figure 4: CV's of 5 mM BH_4^- in 1 M NaOH at Pt (black line) vs. CV of Pt in 1 M NaOH without any fuel present (blue line).

We found that BH_4^-'s two reaction mechanisms at Pt seem to be intricately tied the state of the Pt surface. A comparison of the anodic sweep of a stationary cyclic voltammogram (CV) of BH_4^- at Pt compared to a CV of polycrystalline Pt in electrolyte alone (1M NaOH) is shown

in Figure 4. The two small peaks at -0.7 and -0.55 V in BH_4^-'s CV overlap perfectly with the positions for surface hydrides (adsorbed hydrogen) at Pt, suggesting that BH_4^-'s low potential reaction may depend on the formation of surface hydrides as intermediates in its oxidation (Reactions 3.a and 3.b).[8]

3.a: $BH_4^- + 2Pt \leftrightarrows Pt\text{-}BH_3 + Pt\text{-}H + e^-$
3.b: $Pt\text{-}H \leftrightarrows Pt + H^+ + e^-$
Reactions 3.a and 3.b

The peak at -0.1 V in BH_4^-'s CV corresponds very well to OH^- adsorption at Pt. This peak in BH_4^-'s CV is also immediately preceeded by a dip in current, which marks the end of the low-potential reaction in the RDE voltammograms (Figure 2). Thus it seems likely that at Pt, at higher potentials, binding of OH^- to the surface decreases the activity of the low-potential BH_4^- oxidation reaction, and that the high-potential reaction proceeds at an OH^- and Pt oxide covered surface.

These mechanistic findings have guided our selection of alternative catalysts for BH_4^- oxidation, as we have targeted metals that support surface hydrogen species, and have paid close attention to effect of oxides on BH_4^-'s oxidation reaction. (see Proposed Research below). They also point to the importance of having a fundamental understanding of the mechanistic details of the electrode reactions in the selection of fuels (and oxidants) for fuel cell applications.

Much to our surprise, we found that while Au had been widely reported not to be active in BH_4^-'s hydrolysis reaction, we noticed copious H_2 bubble formation at Au's surface as soon as BH_4^- oxidation began (Figure 2). In contrast, BH_4^- oxidation at Pt occurred hydrolysis-free during the low potential reaction, and did not begin until the onset of the higher-potential reaction at -0.1 V. Pt's low-potential reaction is therefore of critical significance to BH_4^- fuel cell operation, as it provides high e^- recovery, high fuel cell voltage (low potential of oxidation), and can proceed free of BH_4^-'s hydrolysis reaction.

Although Pt's low-potential BH_4^- oxidation offers a tremendous gain for BH_4^- fuel cells, it also undergoes an undesirable, though reversible, poisoning reaction. The current was found to decrease by 50-90% within 10-20 min, depending on potential. Similarly, Au also exhibited poisoning behavior with a 40% loss in current over 15 min.

However, we were able to develop a cleaning protocol, based on our RDE study of BH_4^- at Pt and Au.[7] We found that by briefly stepping the potential to +0.60V we could recover virtually all of the electrocatalytic activity. In essence, the $7e^-$ BH_4^- oxidation at Pt was well-maintained for over 20 min, while stepping positive for only 0.5 s every 300s (Figure 5). That is, the potential of the electrode remained at -0.7 V for 600 times the length of time it was held at +0.6 V. The procedure was also successfully applied to an Au electrode held in Au's low potential region (-0.4 V), though the electrode spent only 200 times as long at low potential as it did at +0.6 V. The preliminary demonstration of these cleaning techniques in an actual BH_4^- fuel cell is discussed in Section E, Performance of BH_4^- / CAN and BH_4^- / $Cr_2O_7^{2-}$ fuel cells, below, and suggests that *in-situ* cleaning is instrumental to operation of BH_4^- fuel

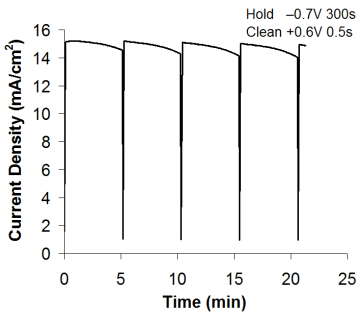

Figure 5: Long-term activity under pulse-cleaning of 5mM BH_4^- in 1M NaOH at Pt, 250 rpm.

cells at high voltage.

Though BH_4^- exhibits appreciable performance at Pt, the cost of a Pt-based fuel cell system will always be of concern. Fortunately, BH_4^- is known to exhibit activity at a number of less precious metals, such as Pd, Ag, Ni, and even misch metals.[9] This feature gives BH_4^- fuel cells an important cost flexibility that is simply unachievable for H_2 or MeOH systems. Preliminary results of BH_4^- oxidation at alternative metal catalysts is discussed below under Proposed Studies.

B. Oxidation of BH_4^- in nonaqueous solvents as a means to address BH_4^- hydrolysis:

While we were able to overcome BH_4^- hydrolysis at electrode catalyst surfaces via the employment of Pt electrodes at low potential, hydrolysis in bulk solution still occurred at high concentrations of BH_4^- (>0.15 M), even in 3M NaOH. This strictly limited the concentrations we were able to test in our fuel cell. Given that $NaBH_4$ has an aqueous solubility of 14.5 M,[10] the current and power densities observed (see Section E below) represent about 1% of that theoretically obtainable from BH_4^-.

Table 1: Solubilities of $NaBH_4$ in organic solvents of varying polarity.

Solvent	BH_4^- Solubility (M)	Comments
DMSO	0.42	
DMF	0.43	
Acetonitrile	-	not soluble
Diglyme	0.46	suspension
Ether	-	not soluble
Methanol	0.33	bubbles
Ethanol	0.49	bubbles
Isopropanol	-	not soluble
1-propanol	-	not soluble
THF	-	not soluble

In an attempt to boost the concentration of BH_4^- in our fuel cell and avoid hydrolysis altogether, we studied the oxidation mechanism of BH_4^- in nonaqueous solvents.[11] First, we assessed a first-order solubility of $NaBH_4$ in a number of solvents of varying polarity (Table 1). We found that many solvents would solubilize $NaBH_4$ above our target of 0.15 M, but most were incompatible with $NaBH_4$. In accord with literature reports, MeOH and EtOH directly reacted with BH_4^-, and performed methanolysis and ethanolysis, respectively, of BH_4^- to H_2.[12,13] These alcohols therefore supplant BH_4^- hydrolysis with equally deleterious reactions. Though $NaBH_4$ is "soluble" in multiple glymes,[14] we found that it made a cloudy suspension, and we concluded BH_4^- would have greatly diminished activity if not fully dissolved. Most of the other, predominantly hydrophobic solvents (i-PrOH, THF) did not appreciably solubilize $NaBH_4$. That left us with just DMSO and DMF as prospective solvents for $NaBH_4$, with solubilities three times higher than we could readily achieve under aqueous conditions (0.42 and 0.43 M, respectively, vs. 0.15 M in water).

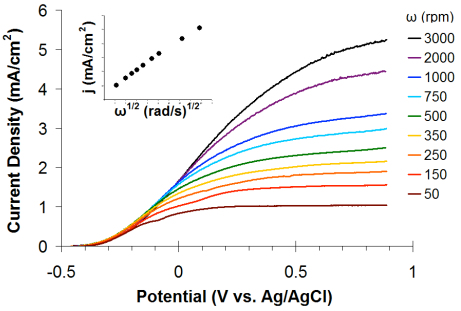

Figure 6: RDE voltammograms of 5mM $NaBH_4$ in DMSO at Pt, with 1M $NaNO_3$ supporting electrolyte.

After finding an appropriate solvent window of stability, $NaBH_4$ was found to exhibit a well-behaved oxidation at Pt in DMSO, without any interference from coupled chemical reactions (Figure 6). The reaction was similar at Au, but with slightly higher overpotential for reaction. In contrast

to DMSO, it was very difficult to obtain reproducible voltammograms in DMF, and slow poisoning over time seemed evident.

Overall, the currents obtained in nonaqueous solvents were disappointingly low, corresponding to an electron recovery of only about 1e$^-$ from BH_4^-, and overpotentials were 0.3 to 0.7 V higher (less favorable) than those observed in base. Voltammograms of 5mM BH_4^- at Pt and Au in 1M NaOH are contrasted with those obtained in DMF and DMSO in Figure 7. The observed currents were ten times lower in some cases, reflecting poor diffusivity of BH_4^- in the solvents in addition to BH_4^-'s lower electron recovery. Literature suggested that methoxy ligands may help stabilize boron in higher oxidation states, and possibly improve electron recovery.[15] However, inclusion of 5 and 30 mM MeOH with 5 mM BH_4^- did not significantly affect current density.

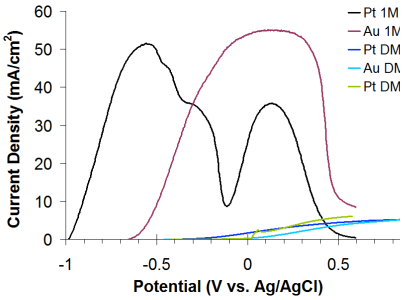

Figure 7: Activity comparison of 5mM BH_4^- in 1M $NaOH_{(aq)}$, DMSO, and DMF at Pt and Au. RDE voltammograms at 3000 rpm are shown.

In addition to these challenges with low current recovery, BH_4^- decomposition to H_2 remained a challenge. While BH_4^- decomposition (hydrolysis) in bulk solution was mitigated via implementation of nonaqueous solvents, BH_4^- still reacted to form H_2 at Pt and Au surfaces during oxidation, with visible H_2 bubble formation. At the moment, nonaqueous solvents do not seem to be a promising avenue for BH_4^- fuel cell research, but further studies in solvents not examined here may help address issues with hydrolysis and decomposition in BH_4^- fuel cells. We also propose physical methods – pressure and confinement – to extend the range of stable concentrations of BH_4^- in aqueous electrolyte.

C. Comparison of previously employed, alternative oxidants for high-power and laminar flow fuel cells

BH_4^- is capable of significant current density in aqueous solutions, producing **0.5 A/cm^2** from just 50 mM fuel when convected (Figure 3, 3000 rpm). In order to balance this reaction in the fuel cell, using a cathode of similar size, highly soluble, kinetically fast oxidants must be employed. O_2, with a maximum solubility of just 1.3 mM, produces a current of around 6 mA/cm^2 at 3000 rpm, falling about two orders of magnitude short of BH_4^-'s current. In order to find a more suitable oxidant for BH_4^-, we examined a number of alternative oxidants that have been employed in fuel cells previously.[7] While various performance parameters for many of these oxidants have already been established, the literature was lacking in a uniform comparison of oxidants tested under identical conditions. Our goal was to provide not only mechanistic information for the various oxidants, but to make a valuable reference highlighting the strengths and weaknesses of each oxidant, allowing other fuel cell researchers to quickly

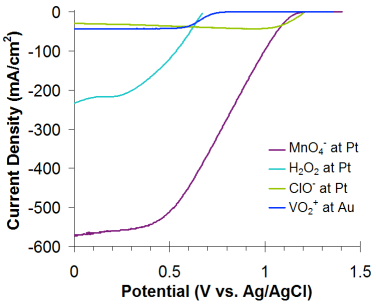

Figure 8: Metacomparison of previously employed oxidants. RDE voltammograms for each oxidant at its best catalyst are shown for 100 mM oxidant in 0.5M H_2SO_4, rotated at 3000 rpm.

compare among fuel cell chemistries.

The oxidants permanganate (MnO_4^-), peroxide (H_2O_2), dioxovanadium (VO_2^+), and hypochlorite (bleach, ClO^-) were studied and compared to O_2. The RDE voltammograms for the reduction of the oxidants at their best catalysts and uniform concentration (100 mM), electrolyte (0.5 M H_2SO_4), and rotation rate (3000 rpm) are shown in Figure 8. Oxidant reduction reactions are shown in Table 2, and the oxidants' mass-transport parameters are summarized in the upper half of Table 3. Each oxidant had a unique blend of transport properties, kinetic character, and mechanistic complexity.

$$2MnO_4^- + 3Mn^{2+} + 2H_2O \rightarrow 5MnO_2 + 4H^+$$
Reaction 4

MnO_4^- had the highest potential and current density of any of the oxidants studied, and was the only oxidant that, at 100 mM, could potentially match BH_4^-'s current density at 50 mM. If paired with BH_4^-, MnO_4^-'s onset potential of +1.2 V would result in an open-circuit voltage of **2.2 V** with a current density > **0.5 A/cm^2**, specific surface area, with convected fuel of just 0.1 M (Figure 8).

Unfortunately, MnO_4^- suffers from a precipitation reaction, which quickly occludes the electrode surface for further reaction at high current densities. It is possible that MnO_4^- could be directly reduced to MnO_2, but this seems unlikely, as this would involve a $3e^-$ transfer (Table 2), while the RDE data was consistent with a $5e^-$ reduction (Table 3). The precipitation is most likely due to MnO_4^-'s $5e^-$ reduction product, Mn^{2+} (Table 2), reacting with excess MnO_4^- to form the intermediate compound MnO_2, a brown precipitate (Reaction 4).[16,17] The concept that the precipitation results from side reactions of MnO_4^-'s reduction product, and is not an inherent feature of MnO_4^- reduction, implies that various measures could be taken to avoid precipitation. For example, sequestration of Mn^{2+} via chelators or other materials would prevent the reaction between Mn^{2+} and MnO_4^-. Our characterization of MnO_4^-'s reduction mechanism to confirm the $5e^-$ pathway has therefore given direction to new approaches for addressing MnO_4^- reduction, and utilizing this remarkably potent oxidizer.

5.a $H_2O_2 \leftrightarrows O_2 + 2H^+ + 2e^-$
5.b $H_2O_2 + 2H^+ + 2e^- \leftrightarrows 2H_2O$
5.c $2H_2O_2 \leftrightarrows 2H_2O + O_2$
Reactions 5.a-5.c

Table 2: Reduction reactions for previously employed and novel oxidants.

Oxidant	Possible Reactions:	E^0 (V vs. Ag/AgCl)
O_2	$O_2 + 2H^+ + 2e^- \leftrightarrows H_2O_2$	0.498
	$O_2 + 4H^+ + 4e^- \leftrightarrows H_2O$	1.032
MnO_4^-	$MnO_4^- + e^- \leftrightarrows MnO_4^{2-}$	0.361
	$MnO_4^- + 4H^+ + 3e^- \leftrightarrows MnO_2 + 2H_2O$	1.482
	$MnO_4^- + 8H^+ + 5e^- \leftrightarrows Mn^{2+} + 4H_2O$	1.310
H_2O_2	$H_2O_2 + 2H^+ + 2e^- \leftrightarrows 2H_2O$	1.579
VO_2^+	$VO_2^+ + 2H^+ + e^- \leftrightarrows VO^{2+} + H_2O$	0.794
	$VO^{2+} + 2H^+ + e^- \leftrightarrows V^{3+} + H_2O$	0.140
ClO^-	$HClO + H^+ + 2e^- \leftrightarrows Cl^- + H_2O$	1.285
	$HClO + H^+ + e^- \leftrightarrows ½Cl_2 + H_2O$	1.414
$Ce(NH_4)_2(NO_3)_6$	$Ce^{4+} + e^- \leftrightarrows Ce^{3+}$	1.523
$S_2O_8^{2-}$	$S_2O_8^{2-} + 2H^+ + 2e^- \leftrightarrows 2HSO_4^-$	1.926
IO_3^-	$IO_3^- + 6H^+ + 6e^- \leftrightarrows I^- + 3H_2O$	0.888
IO_3^-	$IO_3^- + 6H^+ + 5e^- \leftrightarrows I_2 + 3H_2O$	0.998
$HCrO_4^-$	$HCrO_4^- + 7H^+ + 3e^- \leftrightarrows Cr^{3+} + 4H_2O$	1.153
$Cr_2O_7^{2-}$	$Cr_2O_7^{2-} + 14H^+ + 6e^- \leftrightarrows 2Cr^{3+} + 7H_2O$	1.035

H_2O_2, like O_2, is only reduced at Pt after Pt's oxide has undergone significant reduction/removal at about +0.65 V vs. Ag/AgCl. At potentials above this value, H_2O_2 is oxidized to O_2. As a result, H_2O_2 provides about 0.5 V less voltage than other oxidants studied. During reduction, H_2O_2 undergoes a catalytic decomposition to O_2 (Reactions 5.a-5.c).[18] This decomposition vigorously produces O_2 gas bubbles at the surface, causing the same disruptions in fluid flow and available electrode area discussed previously for H_2 production during BH_4^- oxidation. The resulting decrease in current and pressurization in a fuel cell makes H_2O_2 very difficult to implement, and our initial fuel cell studies using H_2O_2 were plagued with low current densities and leaks. Aside from this side reaction, H_2O_2 has a high diffusion coefficient and two e^- per molecule, resulting in a substantial current density of **0.22 A/cm^2**. Because H_2O_2 is fully miscible in water, and is a liquid in its pure state, it can be brought to very high concentration, which would otherwise allow for a significant scale-up of its current density in a practical device. In moving forward, as with BH_4^-, we propose strategies to exploit H_2O_2 at high concentrations.

Table 3: Mass transport parameters relevant to current density for previously employed and novel oxidants.

	Oxidant	# of e^-	Diffusion Coefficient ($x10^{-5}$ cm^2/s)	Solubility (M)	Current Density* (mA/cm^2)	Complication
Previously Employed Oxidants (Increasing Current Density)	$NaMnO_4$	5	1.2	7.3	560	Precipitation
	H_2O_2	2	1.5	42.4	220	Bubbles
	VO_2^+	1	0.25	< 3†	43	Reversible Poisoning at Au
	NaClO	1?	1.1	10.7	> 50	Irreversible Poisoning at Pt, Au, GC
	O_2	4	1.3	< 0.001	6.2	
Novel Fuel Cell Oxidants (Increasing Current Density)	$Na_2Cr_2O_7$	6	0.8	7.1	540	Oscillations, Poisoning
	$NaIO_3$	5-6?	1.1	0.5	340	
	Na_2CrO_4	3	0.92	5.4	290	
	$Na_2S_2O_8$	2	0.6	2.3	150	
	CAN	1	0.42	2.6	57	

The mass-transport limited current density for 100 mM of the given oxidant at 3000 rpm is shown.
VO_2^+ is typically generated from the precursor VO^{2+}, so the solubility for $VOSO_4$ is shown.

VO_2^+ is a specialty oxidant seen essentially exclusively in vanadium "redox batteries," or reversible vanadium fuel cells.[19] The primary advantage of such systems is the reversibility of the redox reactions and the simplicity of having vanadium in both positive (VO_2^+ and VO^{+2}) and negative (V^{+3} and V^{+2}) half-cell reactions. Aside from its ability to be used in reversible charge-storage systems, VO_2^+ is lacking in many important features for fuel cell applications. It participates in just a $1e^-$ transfer reaction and has low solubility (< 3 M, Table 3), and so has a strictly limited maximum possible current density. We also found VO_2^+ to have a remarkably low diffusion coefficient[20] that is four times lower than any of the other oxidants studied, and is two to six times lower than most known soluble species in general.[10] This combination of mass transport parameters gave VO_2^+ the lowest current density of the alternative oxidants in our comparison. Factoring in VO_2^+'s relatively lower onset potential for reduction (about 0.5 V lower than MnO_4^-, Figure 8), it is unlikely that VO_2^+ will play a role in high power density fuel cells.

That said, we did find that the power density of vanadium redox battery systems can probably be increased significantly by switching cathode material from glassy carbon (GC) to Au. Most vanadium systems use carbon-based cathodes to decrease cost. However, the onset potential and $E^{1/2}$ for reduction are shifted positive by 0.6 V at Au (Figure 9), indicating a 0.6 V gain in both open-circuit and operating voltages for vanadium fuel cells that use Au cathodes. Previously, it was determined that VO_2^+ would slowly poison Au cathodes,[20] but we discovered that occasionally pulsing the electrode to high potentials (> +0.6 V vs. Ag/AgCl, 0.5 M H_2SO_4) would remove surface-bound poisons and fully restore current density in a manner analogous to our findings with BH_4^-.

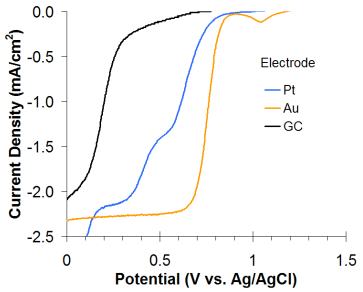

Figure 9: RDE voltammograms of 5mM VO_2^+ in 0.5M H_2SO_4 at Pt, Au, and glassy carbon, 3000 rpm, cathodic sweeps at 20 mV/s.

ClO^- has only recently appeared as a fuel cell oxidant,[21,22] and we were understandably skeptical of its effectiveness. It is expected for ClO^- to be reduced to either $Cl_{2(g)}$ or Cl^- (Table 2), the latter of which is a well-known poison for noble metals. Poisoning was indeed evident in our study. In fact, ClO^- reduction poisoned Pt so quickly that we were unable to complete a single RDE voltammogram without significant loss of current during the scan (Figure 8). ClO^- reduction poisoned Au as well, and even glassy carbon. It is unclear to us why the poisoning was not noticed by other researchers. It is possible that, in some cases, the electrodes used may have been pre-poisoned by the use of Cl^- electrolytes.[21] Other fuel cells used high-surface area electrodes,[22] and complete poisoning may not have occurred on the time scale of the experiment.

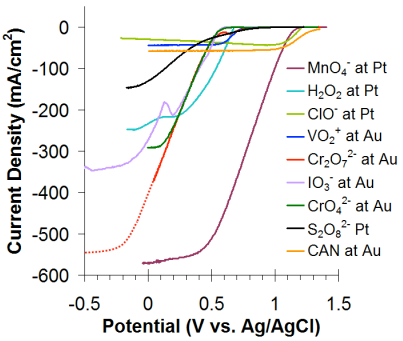

Figure 10: Metacomparison of conventional and new oxidants. RDE voltammograms for 100 mM oxidant at its best catalyst in 0.5M H_2SO_4, rotated at 3000rpm, are shown.

Aside from its undesirable reaction products, ClO^- reduction served as a potent process. The reduction itself occurred at exceptionally high potentials at Pt (+1.2 V, Figure 10), practically at the limit of an aqueous system, allowing for a very high voltage fuel cell. Though only $1e^-$ is involved in the reduction, NaClO has very high solubility (10.7 M, Table 3), which would allow for significant scale-up of the process.

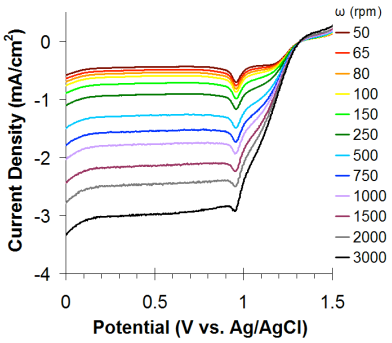

Figure 11: RDE of 5mM CAN in 1M HNO_3 at Au.

Unlike MnO_4^-, unfortunately, ClO^-'s poison formation is inherent to the reduction of the oxidant itself, and will probably be difficult to avoid. We do not think that ClO^- will be a candidate oxidant for future fuel cells.

D. Investigation of novel, superior oxidants for high-power and laminar flow fuel cells

Because none of the alternative oxidants studied were ideal, we instead turned to novel oxidants not previously employed in fuel cell devices. From an array of known oxidant reduction reactions, we chose those that we thought would be the most promising. Cerium ammonium nitrate, $Ce(NH_4)_2(NO_3)_6$ (hereafter CAN), and persulfate, $S_2O_8^{2-}$, both have exceptionally high potentials for reduction, and could possibly contribute to high voltage fuel cells (Table 2). CAN was also reported to have a facile kinetic rate of reduction,[23] so it is expected to deliver higher current with a minimal voltage penalty. Based on our studies of alternative oxidants, the number of e^- transferred in the reaction is the most critical factor in determining the limiting current density of a given oxidant. Thus iodate, chromate, and dichromate were chosen because they undergo reductions involving 3 or more electrons (Table 2), and so should provide significant current densities. The RDE voltammograms for the various novel oxidants are shown alongside those for the previously employed oxidants in Figure 10.

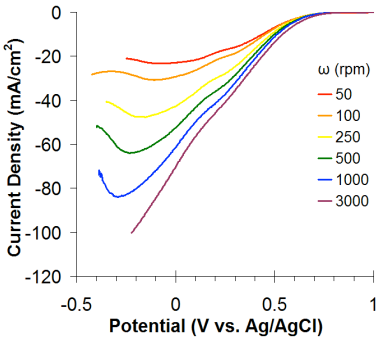

Figure 12: RDE voltammograms of 100mM $S_2O_8^{2-}$ in 0.1M $HClO_4$ at Au.

CAN was one of the best behaved oxidants we worked with, and as a result, was the most extensively studied for our fuel cell work (see Section E, Performance of BH_4^- / CAN and BH_4^- / $Cr_2O_7^{2-}$ fuel cells). At Au, CAN's reduction began immediately negative that of destructive Au etching and dissolution (about +1.3 V), providing a high potential (high voltage) reaction at the limit of the electrode's stability in aqueous solution (Figure 11). Kinetics were rapid, as described in the literature.[23] Perhaps most importantly, the reduction of CAN did not show any interference whatsoever from poisoning or other disadvantageous side reactions, allowing for immediate implementation of CAN into laminar flow fuel cells.

Though CAN's expected voltage is high, its gravimetric energy density and current density are low. For the weight of a lanthanide series metal, only $1e^-$ is delivered (Table 2). In addition to this low electron delivery, CAN also has a diffusion coefficient two and a half times lower than the other oxidants studied (~$0.42x10^{-5}$ cm^2/s[23,24], Table 3), on par with VO_2^+'s. Also like VO_2^+, CAN has a low solubility, precluding effective scale-up of the oxidant. While CAN proved easy to work with in our fuel cell, oxidants with higher current densities were sought to further increase power density.

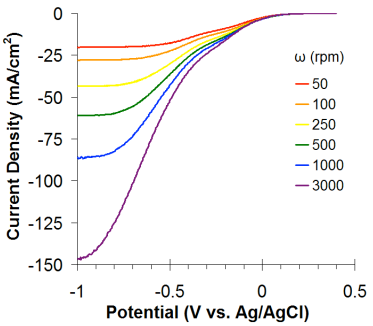

Figure 13: RDE voltammograms of 100 mM $S_2O_8^{2-}$ in 1M NaOH at Pt.

With an E^0 of +1.926 V, $S_2O_8^{2-}$ had the highest standard potential of any oxidant studied, and combined with its $2e^-$ reaction (Table 2), it appeared very promising for delivering both voltage and

current. However, like many of the compounds we studied (such as BH_4^- at Au and H_2O_2 at Pt), the thermodynamics were not realized in an electrochemical setting. At Au in 0.1 M $HClO_4$, $S_2O_8^{2-}$ does not begin its reduction until +0.7 V (Figure 12), consistent with literature results,[25] and its reaction kinetics were rather slow at every pH, electrolyte, and catalyst studied. Utilizing $S_2O_8^{2-}$ reduction is difficult, as it is thought to undergo a dissociative adsorption to form adsorbed SO_4^{2-} at Pt surfaces, and the adsorbed SO_4^{2-} blocks Pt for further reaction until SO_4^{2-} is removed at very low potentials.[26,27] Our data supported this concept, showing mostly a self-poisoning peak at Pt. Some researchers have speculated that OH^- enhances $S_2O_8^{2-}$'s reduction reaction,[25,27] and our results confirmed that $S_2O_8^{2-}$ reduction will proceed to a mass-transport limited current at Pt in 1 M NaOH (Figure 13). Of course, switching from acidic to basic medium shifts pH dependent reactions negative by ~0.8 V (0.059 V per pH unit via the Nernst equation[28]), so the potential of the reduction becomes significantly less attractive using this approach.

Despite these drawbacks, $S_2O_8^{2-}$, like CAN, did not appear to undergo any deleterious side reactions or poisoning at Au in acid, and can therefore find immediate utility in fuel cells. Though its onset potential for reduction was much lower than expected, it was still reasonably high, on par with H_2O_2 and O_2, and could produce significantly higher current than CAN (Figure 10). Many fuel cell researchers currently using H_2O_2, who are frustrated with O_2 bubble formation, can obtain trouble-free operation with only a moderate decrease in activity by switching to $S_2O_8^{2-}$, especially if low overpotentials are used.

IO_3^- was a very attractive oxidant, with expected reductions involving 5 and $6e^-$ (Table 2). Indeed, IO_3^- produced the third-highest limiting current of any of the oxidants studied (0.35 A/cm^2, Figure 10). Complications quickly arose, though, when assessing current delivered over time. Oscillatory behavior manifested, in which the reaction seemed to switch between the 5 and $6e^-$ processes. The process repeated in a cyclical pattern for several minutes, while the overall current slowly diminished. A similar process has been described under galvanostatic conditions,[29] and may be akin to the Briggs-Rauscher "iodine clock" experiment.

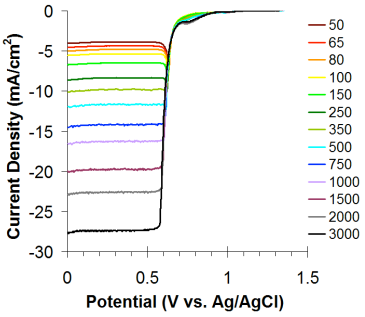

Figure 14: RDE voltammograms of 5mM $Cr_2O_7^{2-}$ in 0.5M H_2SO_4 at Au.

The highest-impact findings of our exhaustive search through novel oxidant chemistries were, by far, the massive current densities afforded by the two chromium species, chromate, CrO_4^{2-}, and dichromate, $Cr_2O_7^{2-}$ (Figure 10). The activities (onset potential, kinetic rate of reaction, etc.) were identical, with the exception that $Cr_2O_7^{2-}$ produced about double the current density of CrO_4^{2-}, in accord with $Cr_2O_7^{2-}$'s doubled number of accepted electrons (6 vs. $3e^-$). $Cr_2O_7^{2-}$ is unique as an oxidant, possessing two transition metal atoms in the same molecule, doubling the current density at a given concentration while preserving fast kinetics. Indeed, we found $Cr_2O_7^{2-}$'s kinetics to be immeasurably fast by RDE methodology, with RDE voltammograms appearing as, essentially, step functions instead of smooth waves (Figure 14).

Like CAN, reduction of $Cr_2O_7^{2-}$ does not appear to have any poisoning or adverse side reactions, and we were able to observe sustained current densities > **0.4 A/cm^2**, specific surface area, for 20 min. Because $Cr_2O_7^{2-}$ accepts 6 times the number of e^- as CAN, and has a diffusion coefficient about twice as large, its current density is nearly ten times greater (Figure 14 vs. Figure 11). Though current is significantly higher, $Cr_2O_7^{2-}$ manifests an onset potential about 0.5 V lower (less favorable) than CAN. When coupling to a low-potential fuel like BH_4^- (-1 V), however, this may represent a voltage drop of only about 20-30% for an order of magnitude gain in cathodic current.

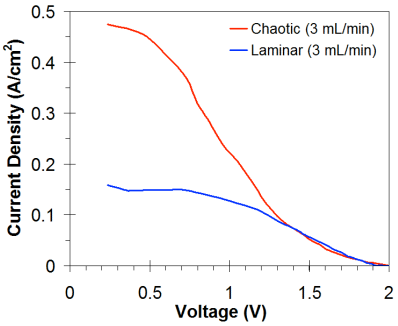

Figure 15: Load Curves for fuel cell using 0.15M $NaBH_4$ in 3M NaOH at Pt, 0.5M CAN in 1M HNO_3 at Pt.

In our search of novel oxidants, $Cr_2O_7^{2-}$ was the oxidant most comparable to MnO_4^-, providing a similar current density of ~**0.5 A/cm^2** at 0.1 M concentration (Figure 10) to match BH_4^-'s current density at just 0.05 M (Figure 3). Though $Cr_2O_7^{2-}$'s reduction does not begin until 0.5 V more negative (less favorable) than MnO_4^-'s, the reaction is free of poisoning and side reactions, allowing it to be implemented today without further investigation or development. Though we have not studied it as thoroughly in our fuel cell as CAN, as we discovered $Cr_2O_7^{2-}$ later in our oxidants search, our preliminary results are in agreement with our analytical RDE investigation, and we are continuing to study fuel cell operation at higher concentrations and power densities (see Section E, Performance of BH_4^- / CAN and BH_4^- / $Cr_2O_7^{2-}$ fuel cells).

E. Performance of BH_4^- / CAN and BH_4^- / $Cr_2O_7^{2-}$ fuel cells

Our BH_4^- / CAN fuel cell combines two reactions occurring at the limit of solvent stability to manifest very high voltages in fuel cells. The convection in our laminar flow fuel cell allows for the use of dual (asymmetric) electrolytes, which can result in a significant increase in the open circuit potential. This arises from the fact that at high pH the potential for fuel oxidation is shifted negative, while in acid the potential for oxidant reduction is shifted positive. With our fuel in 1 M NaOH and our oxidant in 1 M HNO_3, the 14 unit pH difference further increases the voltage by ~0.84 V, as predicted by the Nernst equation (0.059 V/pH unit[28]). Thus we achieved open-circuit potentials of >2 V (Figure 15), about 0.8 V greater than the traditional 1.2 V limit obtainable in aqueous solutions. This open-circuit potential value is in very close agreement with the difference in analytically obtained onset potentials for fuel and oxidant (-1 V for BH_4^- at Pt in 1 M NaOH, +1.2 V for CAN in 1 M HNO_3, Figures 2 and 11).

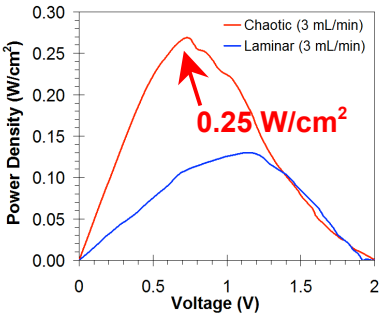

Figure 16: Power Curves for fuel cell using 0.15M $NaBH_4$ in 3M NaOH at Pt, 0.5M CAN in 1M HNO_3 at Pt.

Under conditions of laminar flow, using just 0.15 M fuel and 0.5 M oxidant, we achieved a current density of 0.15 A/cm^2 (Figure 15) and a power density of 0.125

W/cm^2 (Figure 16). Using the chaotic mixers described in Section F, mass transport to the electrodes tripled, in agreement with our theoretical predictions,[30] and therefore tripled our transport-limited current density to nearly **0.5 A/cm^2**. However, because more voltage had to be sacrificed to drive reaction rates faster to support this current density, via Butler-Volmer kinetics,[28] the power doubled, instead of tripled, to **0.25 W/cm^2**.[31] This, however, represents a remarkable achievement in terms of power density.

Performance comparison with other high power fuel cells in the literature is difficult, as other groups use high-surface area electrodes but normalize to geometric area. By normalizing outputs to catalyst loading, our system achieved the highest power density yet recorded for a non-H_2 fuel cell. Whereas MeOH and BH_4^- fuel cells use 1.5-3 M fuel at 60°C and provide up to 30 and 220 mW/mg catalyst, respectively,[9,32] our system used 0.15 M fuel at room temperature and produced **1,230 mW/mg Pt** (Figure 17). This value represents a **50% increase** in Pt utilization from a typical H_2/O_2 fuel cell (800 mW/mg Pt[33]).

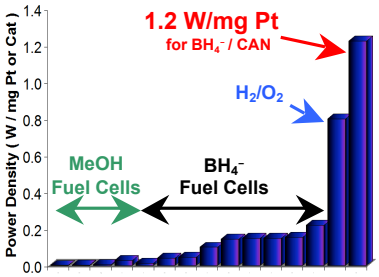

Figure 17: Specific power density normalized to weight of catalyst for BH_4^- / CAN fuel cell vs. other reported and common fuel cells.

The preliminary results from our $BH_4^-/Cr_2O_7^{2-}$ fuel cell indicate that this power density can be pushed many times higher. Under conditions of laminar flow, and fuel limitation, 15 mM BH_4^- in 1 M NaOH at Pt and 20 mM $Cr_2O_7^{2-}$ in 0.5 M H_2SO_4 at Au generated a current density of 60 mA/cm^2 and 50 mW/cm^2 (Figures 18 and 19, respectively). If these performance values scale proportionately when increasing the concentrations of the fuel and oxidant ten times to 0.15 and 0.2 M, similar to the BH_4^- / CAN system, it would produce 0.5 W/cm^2 under laminar flowIn our proposed work, we aim to stabilized BH_4^- out toward its solubility limit (14 M) and reduce the internal resistance of our planar FC. In this limit, we can look toward current and power densities upward of 10 A/cm^2 and 10 W/cm^2.

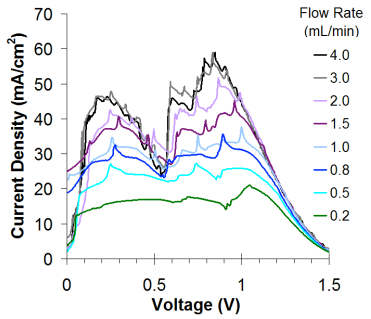

Figure 18: Load curves for fuel cell using 0.015M $NaBH_4$ in 3M NaOH at Pt / 0.02M $Na_2Cr_2O_7$ in 0.5M H_2SO_4 at Au. Laminar flow only.

Furthermore, in our $BH_4^-/Cr_2O_7^{2-}$ fuel cell, we performed a cursory investigation of pulse cleaning to avoid BH_4^- poisoning at Pt, allowing for sustained $7e^-$ current at low anode potential (high fuel cell voltage), as described in Section A, "*Electroanalytical investigation of BH_4^-*". Repeatedly pulsing the potential of the anode to the region of Pt oxide formation successfully enabled sustained currents of 50-60 mA/cm^2 for about 60 min, as predicted by our analytical results (Figure 5). We will perform longer-term studies of BH_4^- fuel cells under pulse cleaning to further demonstrate durability and reliability of the fuel oxidation reaction.

It is notable that pulse cleaning of our $BH_4^-/Cr_2O_7^{2-}$ fuel cell does not consume any outside energy. In Figure 18, the fuel cell load curve closely mirrors the RDE voltammogram of BH_4^- oxidation seen in Figure 2, indicating that the fuel cell is

completely fuel limited at all potentials. In this configuration, the high potential of the oxidant can pull the potential of the anode well into an electrode-cleansing region of Pt oxide, which occurs near the short-circuit current (0 V) in Figure 18. Thus only temporarily decreased current, rather than outside energy, is all that is necessary for the fuel cell to self-cleanse.

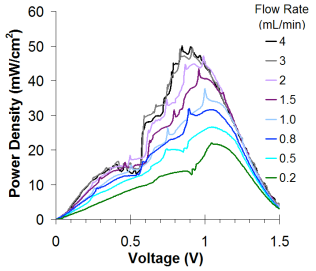

Figure 19: Power curves for fuel cell using 0.015M $NaBH_4$ in 3M NaOH at Pt / 0.02M $Na_2Cr_2O_7$ in 0.5M H_2SO_4 at Au. Laminar flow only.

F. Enhancement of rates with three-dimensional laminar flows

Our analysis predicts[34,35] that the introduction of three-dimensional (3-D) flows within laminar systems can provide significantly higher rates of interfacial transfer. To test our predictions quantitatively, we have worked in microfluidic potential cells (Figure 20(a)) with structured electrodes (Figure 20(b)). Figure 20(C) presents the rates of mass transfer as the average Sherwood number, Sh_{ave} ($Sh = k_M H/D$, where k_M is the mass transfer coefficient, H is the characteristic dimension of the channel, and D is the diffusivity of the reactive species). Measurements are shown for smooth electrodes (triangles), grooved electrodes that generate non-chaotic flow (circles), and grooved electrodes that generate chaotic flow (crosses and squares)[36]. For the stirred, non-chaotic flow, the grooved boundary acted as the counter electrode (circles); for the chaotic flow, the grooved boundary acted as both the counter (crosses) and the working electrode (squares). These measurements demonstrate the following important points: 1) the induction of either chaotic or non-chaotic flow adjacent to a reactive boundary can significantly increase transport-limited current relative to an unstirred, laminar flow. When the stirring is induced from the counter, this increase is ~2-fold (circles and crosses vs. triangles); when the stirring is induced from the working electrode, the increase is ~8-fold (squares vs. triangles). 2) In stirred flows, the entrance length is short and Sh goes to a Pe-dependent, asymptotic value, Sh_{aym} that can be much greater than one. This behavior can be seen by the absence of the constant region at low Pe for the stirred flows. 3) The measured rates match quantitatively with the predictions of our modified Grætz theory[34,35] with no adjustable parameters: the prefactors of the best fits lines in Figure 20(c) match the predictions within 20%; the exponents (-1/3) are those predicted.

This solid theoretical basis and the extremely high rates achievable with structured electrodes will serve us well as we develop methods to exploit our fast, high concentration fuels and oxidants. We note that for $Sh_{ave} = 40$ in a channel of depth, $H = 50$ μm and a typical diffusity ($D = 10^{-9}$ m^2/s), we can achieve a mass transfer coefficient, $k_M = 8\times10^{-2}$ cm/s, a value that is comparable the kinetic rate constants measured for our fast fuels and oxidants ($k > 0.02$ cm/s)[6,7] To take full advantage of these rates and the high energy densities of our fuels and oxidants in this format, we propose to develop methods to stabilize high concentration solutions of BH_4^- (and H_2O_2) and incorporate rigid flow separators with high ionic conductance.

G. Reactive bubbly flow in Fuel Cells

In meeting the challenge of combining high power density with high fuel efficiency, the fuel/oxidant couple $NaBH_4/H_2O_2$ is a very good candidate with a theoretical high open circuit voltage of 3V (Reaction 1, Table 2) and high current density (Figures 3 and 8). However, as mentioned earlier, H_2O_2 reacts via a catalytic decomposition (Reaction 5.c) to form bubbles at the electrode surface, resulting in reduced area available for mass transfer and fuel/oxidant crossover. These phenomena adversely affect the power output of the fuel cell system. In order to overcome these challenges, we have conducted experiments to study the different multiphase flows present in the fuel cell. This study is aimed at managing the multiphase flow to achieve spontaneous stirring of the reagent streams to meet the challenges of high power density and high fuel utilization efficiency. We report here our progress toward the characterization and understanding of the fluid dynamics in these reactive multiphase flows. Below, we propose approaches to exploit this knowledge for the development of multiphase FCs that can exploit the exceptional kinetics and energy density of $NaBH_4$ and H_2O_2.

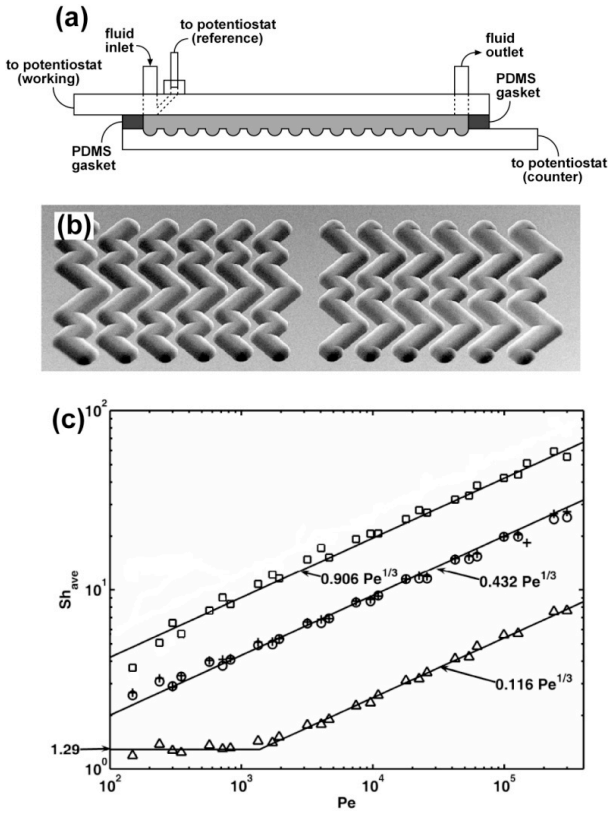

Figure 20. Electrochemical measurements of rates of mass transfer in microfluidic potential cells. **(a)** Schematic diagram of microfluidic potential cell. Top and bottom walls of channel act as working and counter electrodes, respectively. Grooves of herringbone mixing structure are indicated on bottom wall. **(b)** Scanning electron micrograph of counter electrode with groves in staggered herringbone motif. **(c)** Globally averaged Sherwood numbers evaluated from measured current for uniaxial flow over smooth counter electrode (triangles), 3-D, chaotic flow over counter with staggered herringbone motif (crosses), 3-D, non-chaotic flow over counter with symmetrical herringbone motif (circles) and over working with herringbone motif (squares). Experiments were run with the reversible redox species, ferricyanide/ferrocyanide run at the transport-limited current.

Experimental Characterization of multiphase flows to study the different regimes in a fuel cell system. In understanding the role of gas-liquid flow for interfacial mass transfer in the fuel cell system, we focused our efforts on characterizing the flow patterns during the catalytic decomposition of H_2O_2 on Pt (reaction 5.c). Developing a map of different flow patterns has been performed for boiling[37] but not for heterogeneous reactive flows. Characterization was done in a microchannel as in Figure 21. The pattern of electrodes in each channel is designed to work like a fuel cell with working and counter electrodes on

the same surface 400 microns apart and was used to clean the surfaces electrochemically within the assembly[38]. The multiphase flow is visualized using a high speed camera.

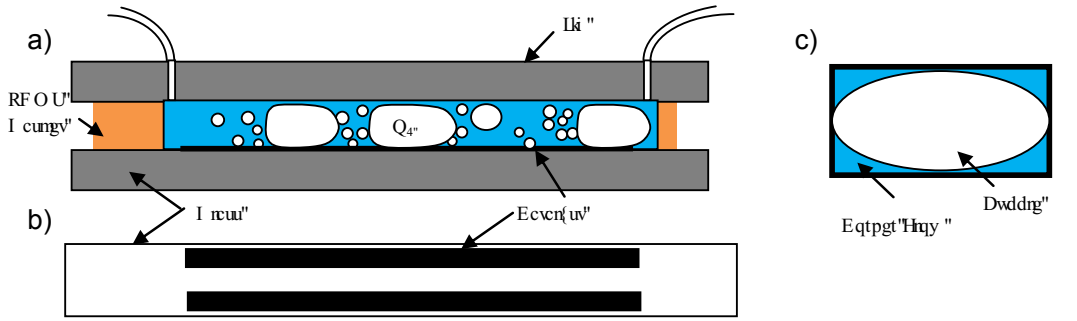

Figure 21: (a) Schematic of the experimental setup - Assembly of the device with the jig, PDMS gasket and the glass patterned with Pt. (b) Patterning of the catalyst in the Ferringo fuel cell geometry. (c) Cross section of the channel with a bubble, showing the corner flow past the bubble.

Experiments were performed by varying the average velocity U and the concentration C_0 of the reactant, H_2O_2. We identify the capillary number, $Ca = \mu U/\sigma$, where μ [kg/m s] is the viscosity, U [m/s] is the average flow speed, and σ [J/m^2] is the surface tension; Ca captures the competition between the viscous and capillary forces defining the dynamics in a bubbly flow and allows for generalization of conclusions. We represent the concentration as a molar flow rate to serve as a measure of the ratio of the gas to liquid volume flow rate. Figure 22(a) shows the flow map we obtained in the system for the parameter space explored. The churn/slug flow (Figure 22(b)) covers most of the parameter space accessed. At higher molar flow rates and higher capillary numbers we find the transition to a regime with dispersed bubbles throughout the channel (churn – Figure 22(b)). At low molar flow rates, transition to a regime with no bubbles occurs. The churn/slug regime approximates the desired Taylor regime that would provide efficient mass transfer and allow for steady operation. However, the length of gas to liquid slugs varies with time as well as with the concentration and capillary number (Figure 23(a)). These variations must be controlled in order to achieve a useful Taylor regime.

Understanding the dynamics of bubble growth, departure, and propagation. To build a basis for engineering these flows, we have further analyzed the dynamics of the growth and departure of bubbles. Figure 23 presents the scaling of the bubble length (a) and the time delay (b) between departures of bubbles from the leading edge of the electrodes. Interestingly, both quantities present robust power-law scaling over a broad range of conditions. The lengths scale as $Ca^{-1/2}$ and are independent of the concentration. This observation indicates a purely hydrodynamic effect (independent of chemical rate) in which the resistance to flow around the bubble grows with its length until the threshold

for break-off from the surface is achieved. This resistance is controlled by the form of

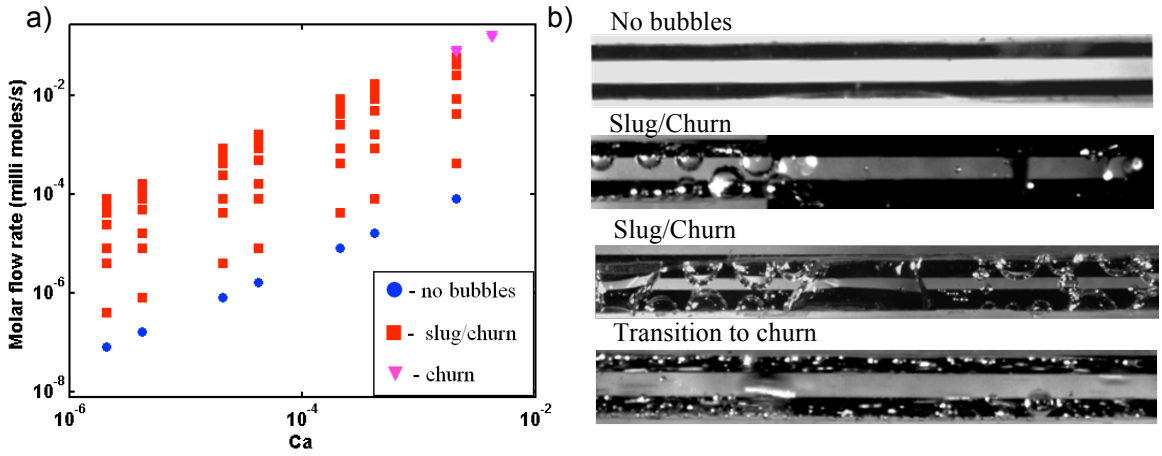

Figure 22: (a) The flow map showing the multiphase patterns for the parameter space explored. (b) The different flow patterns over different values of *Ca* number are shown on the right.

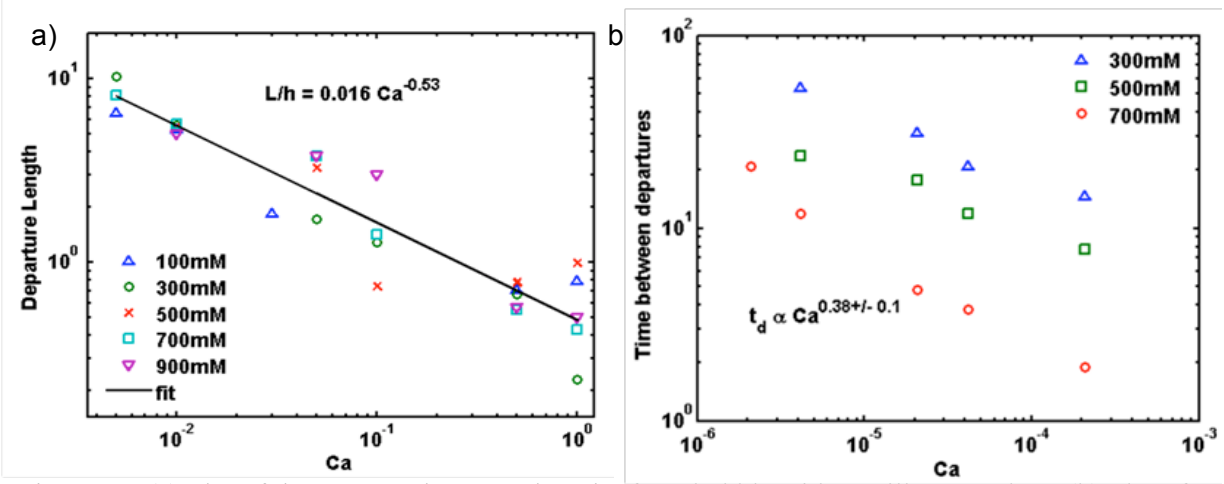

Figure 23: (a) Plot of the average departure length of gas bubble with Capillary number. (b) Plot of the average time between departures of two bubbles with Capillary number.

the liquid channels that surround the bubble (Figure 21(c)) [39 40]; this observation points to an opportunity to manipulate this behavior by changing the shape of the channel's cross-section. The time delay scales as $Ca^{-1/3}$ and exhibits dependence on the concentration. This observation indicates that the growth of the bubble is controlled by the mass transfer-limited rate of decomposition of H_2O_2 to O_2. This process cannot be manipulated independently of the operation of the electrochemical process. Below, we propose to introduce regulation of the absolute pressure imposed on the flow in order to manipulate the relative volumes of the gas (compressible) and liquid (incompressible) phases. The introduction of this additional variable, when coupled with the robust dynamics that we have elucidated, will allow us to navigate the distinct flow regimes more freely and thus access the desired Talyor regime (Figure 26).

REFERENCES:

1) J.H. Morris, H.J. Gysling, and D. Reed, *Chemical Reviews* **1985**, *85*, 51.
2) R.L. Pecsok, *J. Am. Chem. Soc.* **1953**, *75*, 2862.
3) M.V. Mirkin, H. Yang, and A.J. Bard, *J. Electrochem. Soc.* **1992**, *139*, 2212.
4) E. Gyenge, *Electrochim. Acta* **2004**, *49*, 965.
5) U.B. Demirci, *J. Power Sources* **2007**, *172*, 676.
6) D.A. Finkelstein, N.D. Mota, J.L. Cohen, and H.D. Abruña, *J. Phys. Chem. C.* **2009**, *113*, 19700.
7) David A. Finkelstein, Joseph D. Kirtland, Nicolas Da Mota, Abraham D. Stroock, Héctor D. Abruña *J. Phys. Chem. C* (2011), **115**(13), 6073-6084.
8) H. Dong, R. Feng, X. Ai, Y. Cao, H. Yang, and C. Cha, *J. Phys. Chem. B* **2005**, *109*, 10896.
9) J. Ma, N.A. Choudhury, and Y. Sahai, *Renewable and Sustainable Energy Reviews* **2010**, *14*, 183.
10) D.R. Lide ed., *CRC Handbook of Chemistry and Physics*, 86th ed. (CRC Press, Boca Raton, FL, 2005).
11) D.A. Finkelstein, D.J. Jones, K. Hernandez-Burgos, and H.D. Abruña, **2011**, *J. Power Sources* (2011), **196**(15), 6223-6227.
12) R.E. Davis and J.A. Gottbrath, *J. Am. Chem. Soc.* **1962**, *84*, 895.
13) D.L. Klayman and T.S. Griffin, *J. Am. Chem. Soc.* **1973**, *95*, 197.
14) H.C. Brown, E.J. Mead, and B.C.S. Rao, *J. Am. Chem. Soc.* **1955**, *77*, 6209.
15) B.A. Hathaway, *J. Chem. Educ.* **1998**, *75*, 1623.
16) F.A. Cotton and G. Wilkinson, *Advanced Inorganic Chemistry*, 4th ed. (Wiley, New York, NY, 1980).
17) K.S. Salloum, J.R. Hayes, C.A. Friesen, and J.D. Posner, *J. Power Sources* **2008**, *180*, 243.
18) V.G. Prabhu, L.R. Zarapkar, and R.G. Dhaneshwar, *Electrochim. Acta* **1981**, *26*, 725.
19) M. Skyllas-Kazacos, M. Rychcik, R.G. Robins, and A.G. Fane, *J. Electrochem. Soc.* **1986**, *133*, 1057.
20) E. Sum, M. Rychcik, and M. Skyllas-Kazacos, *J. Power Sources* **1985**, *16*, 85.
21) M.G. Medeiros and E.G. Dow, *J. Power Sources* **1999**, *80*, 78.
22) E. Kjeang, R. Michel, D.A. Harrington, D. Sinton, and N. Djilali, *Electrochim. Acta* **2008**, *54*, 698.
23) P. Kiekens, L. Steen, H. Donche, and E. Temmerman, *Electrochim. Acta* **1981**, *26*, 841.
24) R. Greef and H. Aulich, *J. Electroanal. Chem.* **1968**, *18*, 295.
25) L.D. Burke, J.F. O'Sullivan, K.J. O'Dwyer, R.A. Scanell, M.J.G. Ahern, and M.M. McCarthy, *J. Electrochem. Soc.* **1990**, *137*, 2476.
26) L. Muller, *J. Electroanal. Chem.* **1967**, *13*, 275.
27) S. Nakanishi, S.I. Sakai, M. Hatou, Y. Mukouyama, and Y. Nakato, *J. Phys. Chem. B* **2002**, *106*, 2287.
28) A.J. Bard and L.R. Faulkner, *Electrochemical Methods*, 2nd ed. (John Wiley & Sons, Inc., New York, NY, 2001).
29) E.V. Radkov and L.G. Ljutov, *J. Electroanal. Chem.* **1988**, *241*, 349.

30) J.D. Kirtland, G.J. McGraw, and A.D. Stroock, *Phys. Fluids* **2006**, *18*, 073602.
31) N.D. Mota, J.D. Kirtland, D.A. Finkelstein, C.A. Rodriguez, A.D. Stroock, and H.D. Abruña, *Submitted.* **2011**,
32) R. Dillon, S. Srinivasan, A.S. Aricò, and V. Antonucci, *J. Power Sources* **2004**, *127*, 112.
33) A.D. Taylor, B.D. Lucas, L.J. Guo, and L.T. Thompson, *J. Power Sources* **2007**, *171*, 218.
34) J.D. Kirtland, G.J. McGraw, and A.D. Stroock, *Physics of Fluids* **2006**, *18*
35) J.D. Kirtland, C.R. Siegel, and A.D. Stroock, *New Journal of Physics* **2009**, *11*
36) J.D. Kirtland and A.D. Stroock, *Annalen der Physik* **2011**, *submitted*
37) P. Cheng, G.D. Wang, and X.J. Quan, *Journal of Heat Transfer-Transactions of the Asme* **2009**, *131* (4)
38) R. Ferrigno, A.D. Stroock, T.D. Clark, M. Mayer, and G.M. Whitesides, *Journal of the American Chemical Society* **2002**, *124* (44), 12930.
39) H. Wong, C.J. Radke, and S. Morris, *Journal of Fluid Mechanics* **1995**, *292*, 95.
40) H. Wong, C.J. Radke, and S. Morris, *Journal of Fluid Mechanics* **1995**, *292*, 71.

6. Publications supported by grant:

Finkelstein D.A., Letcher C.D., Jones D.J., Sandberg L.M., Watts D.J., Abruña H.D. (2013) Self-poisoning during BH – oxidation at Pt and Au, and *in-situ* poison removal procedures for BH4– fuel cells. *J. Phys. Chem. (2013) C.*, *117*, 1571-1581.

Sundararajan, Pavithra; Stroock, Abraham D. "Transport Phenomena in Chaotic Laminar Flows" Annual Review of Chemical and Biomolecular Engineering (2012), 3, 473-496.

P. Sundararajan, J. D. Kirtland, D. L. Koch, and A. D. Stroock Impact of chaos and Brownian diffusion on irreversibility in Stokes flows PHYSICAL REVIEW E 86, 046203 (2012)

Da Mota N., Finkelstein D.A., Kirtland J.D., Rodriguez C., Stroock A.D., Abruña H.D. Membraneless, room-temperature, direct borohydride/cerium fuel cell with power density of over 0.25 W/cm2. *J. Am. Chem. Soc.*, (2012) *134*, 6076-6079.

Finkelstein D.A., Jones D.J., Hernandez-Burgos K., Abruña H.D. Electro-oxidation of BH4– in dimethylsulfoxide and dimethylformamide studied by rotating disk electrode voltammetry. *J. Power Sources*, (2011) *196*, 6223-6227.

Finkelstein D.A., Kirtland J.D., Da Mota N., Stroock A.D., Abruña H.D. 2 (2011) Alternative oxidants for high-power fuel cells studied by rotating disk electrode (RDE) voltammetry at Pt, Au, and glassy carbon electrodes. *J. Phys. Chem. C. (2011)*, *115*, 6073-6084

Kirtland, J.D.; Siegel, C.R.; Stroock, A.D. Interfacial mass transport in steady three-dimensional flows in microchannels. *New Journal of Physics*. 11, 075028 (2009).

Finkelstein D.A., Da Mota N., Cohen J.L., Abruña H.D. (2009) Rotating 46 disk electrode investigation of BH_4^- and BH_3OH^- Electro-oxidation at Pt and Au: Implications for BH_4^- Fuel Cells. *J. Phys. Chem. C.*, (2009) *113*, 19700- 19712.

Kirtland, Joseph D.; Siegel, Corey R.; Stroock, Abraham D. "Interfacial Mass Transport in steady three-dimensional flows in microchannels" New Journal of Physics (2009), 11(July)

Jamie L. Cohen, David J. Volpe, Héctor D. Abruña; "Electrochemical determination of activation energies for methanol oxidation on polycrystalline platinum in acidic and alkaline electrolytes", *Phys. Chem. Chem. Phys.* (2007), **9**(1), 49-77.

Kirtland, J. D.; McGraw, G. J.; Stroock, A. D., Mass transfer to reactive boundaries from steady three- dimensional flows in microchannels. *Physics of Fluids*, 18, (7), 073602 (2006).

Jamie L. Cohen, David J. Volpe, Daron A. Westly, Alexander Pechenik, Héctor D. Abruña; "A Dual Electrolyte H2/O2 Planar Membraneless Microchannel Fuel Cell System with Open Circuit Potentials in Excess of 1.4 V", *Langmuir* (2005), **21**(8), 3544-3550.

Jamie L. Cohen, Daron A. Westly, Alexander Pechenik, Héctor D. Abruña; "Fabrication and preliminary testing of a planar membraneless microchannel fuel cell", *J. Power Sources* (2005), **139**(1- 2), 96-105.